



Experimental Characterization of the Rotational Capacity of Hollow Structural Shapes

Elsy Saloumi¹, Marielle Hayeck², Joanna Nseir³, Nicolas Boissonnade⁴

Abstract

The present paper details bending tests on Rectangular Hollow Sections (R.H.S.) and square hollow sections (S.H.S.). The tests primarily aimed at providing information on ultimate load carrying capacities as well as rotations and curvatures in the inelastic range at plastic hinges locations. These bending tests were designed to investigate reserve capacities and plastic redistribution at the plastic-compact border (“class 1-2 border” in Eurocode 3) with the intention of characterizing the demand vs. availability equation in terms of rotational capacity. They consisted in series of 2.60 m to 4.8 m span tests, under various configurations: simply-supported with either 3-point or 4-point bending static systems, or propped cantilever configurations with mid-span and outer-loaded point loads. Several cross-section shapes and dimensions (both external dimensions and thickness) were varied. Geometric and material properties were carefully measured and stub column tests have been performed in order to characterize the level of available ductility of the sections in compression as well. The observed behavior and results of the bending tests show highly variable rotational capacities, and that in most cases the possibility to resort to plastic analysis is disputable for class 1 sections.

1. Introduction

Hollow Structural Shapes (H.S.S.) may be manufactured by means of various technological processes including hot-rolling, cold-forming, welding plates together etc... H.S.S. are becoming widely used in a large range of structural applications for their static, esthetic and functional advantages. Indeed, hollow sections steel beams do not exhibit lateral torsional buckling so that when bent about major-axis, overall buckling does not occur, and the only buckling mode which may affect the resistance is local buckling.

Plastic design is based on the elastic-plastic behavior of the material and on the assumption that flexural members should possess sufficient plastic deformation capacities while maintaining the plastic moment M_p in order to develop collapse mechanism resulting from sequential development of plastic hinges (Bruneau & al. 2011). To allow a full redistribution of bending moments in the structure, plastic hinges must be able to rotate without losing the bending capacity of the sections. In Eurocode 3, to ensure sufficient rotational capacity, width-to-thickness ratios are prescribed. This is meant as being an indirect condition on rotational capacity

¹ Graduate Student, University of Applied Sciences of Western Switzerland, <elsysaloumi@gmail.com>

² Graduate Student, University of Applied Sciences of Western Switzerland, <marielle_hayeck@hotmail.com>

³ Graduate Student, University of Applied Sciences of Western Switzerland, <joanna.nseir@gmail.com>

⁴ Professor, University of Applied Sciences of Western Switzerland, <nicolas.boissonnade@hefr.ch>

(i.e. ductility) through cross-section elements (plates) local slenderness. For a class 1 cross-section, the plastic moment resistance is assumed to be reached and maintained with sufficient rotation capacity to allow redistribution of moments in the steel frame; the section is expected to develop a minimum rotation capacity $R_{cap} = 3$ before the onset of local buckling. The local buckling limits which are in use were derived, mainly in the sixties and seventies, from simple plate-models.

In the practice of plastic design of structures, ductility is defined as the capacity of a structure to undergo deformations after reaching its initial yield without any significant reduction in ultimate strength. The rotation capacity is defined as in Eq. 1, where θ represents the beam end sections rotations and its limit values θ_{pl} , θ_u and θ_{max} are defined in Fig. 1 below.

$$R = \frac{\theta_u - \theta_{pl}}{\theta_{pl}} \quad (1)$$

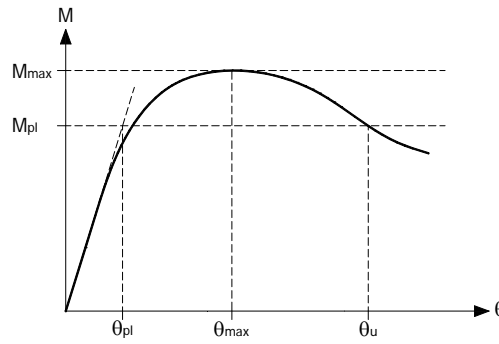


Figure 1: generalized moment-rotation curve

Present research investigations take place in a more global and ambitious context, which aims at developing new and innovative practical design approaches (Boissonnade 2013). As a particular point, these developments call off the usual concept of cross-section classes that, in Europe, also contains a criterion allowing the use of a plastic analysis.

Since this information disappears with the development of the O.I.C. approach, the need to reintroduce or re-asses such criteria is obvious. In particular, this constitutes an opportunity to develop effective and accurate formulations to predict the rotation capacity of hollow beams in order to overcome the inconsistencies of the present codes, which only rely on the limitation of local slenderness for flanges and webs while many other key parameters such as section slenderness, shear, yield strength, moment gradient, ... are disregarded. In order to complement and improve the current knowledge on these particular aspects, extensive research works are presently under development, including experimental, numerical and theoretical development.

This paper describes experimental activities on bending tests on H.S.S. aimed at characterizing the behavior and collapse of class 1 and 2 sections, as well as to serve as a reference for the assessment of finite element shell models that will, in turn, be extensively used in numerical parametric studies. Experimental activities presented herein include several cross-section shapes and dimensions; in a first step, geometrical and material properties were measured and stub column tests performed to measure the level of available ductility of the sections in compression. Then specimens were tested in bending though 4 different configurations: 3-point bending and 4-

point bending with a 2.6 m span length, propped cantilever with mid-span and outer loaded point loads with a 4.8 m span.

2. Experimental program

2.1. General description

The test program undertaken at the University of Applied Sciences Western Switzerland consisted in bending tests on hollow structural shapes (either rectangular R.H.S. or square hollow sections S.H.S.) so as to provide an experimental reference on the inelastic behavior of such members: ultimate load carrying capacity, rotation capacity...

Four different test setup configurations were used: 3-point and 4-point bending static systems with a span length of 2.6 m, propped cantilever configurations with mid-span and outer loaded point loads with a span length of 4.8 m. Six different cross-sections were considered, all corresponding to class 1 sections according to Eurocode 3 classification. Tested beams were fabricated using a hot-formed process, and the steel grade was S355.

6 m profiles were received at the laboratory of Structural Engineering, from which a 400 mm sample was kept for tensile tests, two 2.8 m pieces were cut for the simple supported configuration or 5 m beams were kept for the propped-cantilever configurations. The specimens' lengths were chosen high enough so that the failure mode would occur predominately by bending with little influence of shear. The actual cross-sectional dimensions of each specimen were carefully measured prior to testing.

2.2. Material properties

Hot formed structural steel members usually exhibit uniform material properties within the entire cross-section owing to their fabrication process. The stress-strain curve for these profiles typically displays a sharply defined yield point and a yield plateau followed by strain hardening. For each of the tested H.S.S. specimens, four tensile coupons were extracted from each flat face. The coupons were 270 mm in length and tested under a constant strain rate of 2.5 mm/min. Some of the tested coupons are shown in Fig. 2, and Fig. 3 plots typical stress strain responses of the tested coupon.



Figure 2: Example of tested coupons

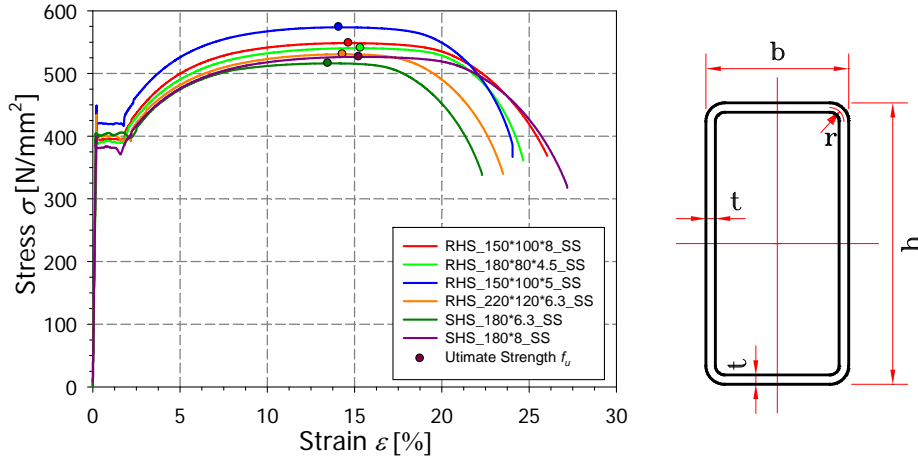


Figure 3: stress-strain curve for RHS_150*100*8_SS coupon

Table 1: Test program summary

Test specimen	h_{mes} (mm)	b_{mes} (mm)	t_{mes} (mm)	L (mm)	f_y (N/mm^2)	f_u (N/mm^2)	E (N/mm^2)	Test configuration
RHS_150*100*8_SS_3P	149.60	99.94	8.35	2600	391	554	205737	Simply supported; 3-point bending
RHS_180*80*4.5_SS_3P	179.35	78.52	4.80	2600	389	539	198504	
RHS_150*100*5_SS_3P	148.97	99.17	5.26	2600	420	573	211215	
RHS_220*120*6.3_SS_3P	217.55	120.75	6.40	2600	396	536	211087	
SHS_180*6.3_SS_3P	179.59	179.59	6.58	2600	393	524	206903	
SHS_180*8_SS_3P	179.44	179.44	7.89	2600	384	532	208013	
RHS_150*100*8_SS_4P	149.48	99.86	8.16	2600	391	554	205737	Simply supported; 4-point bending
RHS_180*80*4.5_SS_4P	179.59	79.71	4.81	2600	389	539	198504	
RHS_150*100*5_SS_4P	149.13	99.48	5.13	2600	420	573	211215	
RHS_220*120*6.3_SS_4P	219.40	120.86	6.42	2600	396	536	211087	
SHS_180*6.3_SS_4P	179.68	179.68	6.68	2600	393	524	206903	
SHS_180*8_SS_4P	179.39	179.39	7.91	2600	384	532	208013	
RHS_180*80*4.5_PR_C	179.19	79.06	4.76	4800	385	527	207854	Propped cantilever; centrally loaded
RHS_150*100*5_PR_C	148.78	99.49	5.20	4800	404	547	213062	
RHS_220*120*6.3_PR_C	219.10	120.45	6.51	4800	393	532	202440	
SHS_180*6.3_PR_C	179.57	179.57	6.72	4800	391	532	206819	
SHS_180*8_PR_C	179.30	179.30	7.94	4800	385	530	213367	
RHS_180*80*4.5_PR_O	178.96	79.45	4.63	4800	387	537	205414	Propped cantilever; off-centrally loaded
RHS_220*120*6.3_PR_O	219.03	120.66	6.51	4800	394	533	210347	
SHS_180*6.3_PR_O	179.55	179.55	6.53	4800	386	529	207744	

Table 1 summarizes the test program and reports on the measured geometric dimensions of all the tested profiles and their main material properties: Young's modulus E , tensile yield strength f_y and ultimate yield strength f_u (the material values reported in Table 1 are averaged values from four coupon specimens cut from the considered section).

3. Stub column tests

Seven stub column tests were performed in order to determine the load carrying capacities under pure compression. The stub columns lengths were chosen as being three times the height of the cross-section to minimize global flexural buckling. Each member length, dimensions and weight were measured prior to testing and were used for the calculation of the measured area assuming a density of 7850 kg/m^3 . The ends of each stub were carefully manufactured, namely regarding flatness (use of a flat marble stone) and horizontality. Two strain gauges have been attached at mid-height of the specimens and on adjacent plates. The testing machine was a 5000 kN hydraulic rig controlled by loading. Two milled flat plates $250 \times 250 \times 150$ of high strength steel ($f_y = 2200 \text{ N/mm}^2$) have been placed on each side of the stub column in order to protect the testing machine surface. Four LVDTs were positioned on the stub ends to record the average end-shortening behavior. The strains gauges indicated if the compression was kept concentrically-applied and provided the load displacement behavior of the specimen in the elastic range, therefore the (indirect) corresponding Young's modulus. The failure shapes of all stub columns are shown in Fig. 4.



Figure 4: General test set-up and failure shapes of stub columns

In order to characterize the test results, cross-sections were first classified according to Eurocode 3 (CEN 2005), for bending and compression load cases. Nominal geometrical dimensions and estimated yield strengths were used; the selected nominal values and corresponding results are shown in Table 2. In bending, all sections are seen to be plastic (class 1); however, cross-sectional classes range from plastic to slender in compression (class 1 to class 4). Plate relative slenderness $\lambda_{rel,p}$ values reported in Table 2 (see Eq. 2) correspond to the maximum relative slenderness value $\lambda_{rel,p}$ of the cross-section constituent plates; in Eq. 2, k is the usual buckling coefficient and $\nu = 0.3$ designates the Poisson's ratio.

$$\lambda_{rel,p} = \sqrt{\frac{f_y}{\pi^2 E} \cdot \frac{12(1-\nu^2)(t/b)^2}{k}} \quad (2)$$

Table 2: Cross-section classification

Test specimen	h	b	t	r	f_y	$(h-t-2r)/$ $t \times \varepsilon$	$(b-t-2r)/$ $t \times \varepsilon$	$\lambda_{rel,p}$ <i>compression</i>	$\lambda_{rel,p}$ <i>bending</i>
	(mm)	(mm)	(mm)	(mm)	(N/mm ²)	(-)	(-)	(-)	(-)
RHS_150*100*8	150	100	8.0	12.00	400	19.2	11.1	0.34	0.20
RHS_180*80*4.5	180	80	4.5	6.75	400	47.0	18.0	0.83	0.34
RHS_150*100*5	150	100	5.0	7.50	420	34.8	21.4	0.61	0.38
RHS_220*120*6.3	220	120	6.3	9.45	400	40.3	19.6	0.71	0.35
SHS_180*6.3	180	180	6.3	9.45	400	32.1	32.1	0.56	0.56
SHS_180*8	180	180	8.0	12.00	400	24.1	24.1	0.42	0.42

Table 3 summaries the obtained results for all stub column tests. For the RHS_180*80*4.5_PR_O, SHS_180*6.3_PR_C, RHS_220*120*6.3_PR_C sections, local buckling was seen to develop unevenly on one side owing to a slightly imperfect flatness on the end sections which resulted in an unexpected moment introduction on the specimen. These experimental defaults as well as other experimental uncertainties may explain why some class 1 or 2 tests have reached ultimate loads slightly below the plastic capacity.

Table 3: Measured properties and ultimate loads of stub columns base profile

Test specimen	<i>Length</i>	<i>Weight</i>	<i>Area</i>	N_{pl}	N_{exp}	N_{exp} / N_{pl}
	(mm)	(kg)	(mm ²)	(kN)	(kN)	(-)
RHS_150*100*8_PR_C	450.5	12.85	3633.6	1440.6	1697.5	1.18
RHS_180*80*4.5_PR_C	541.0	9.50	2237.0	861.6	822.7	0.95
RHS_180*80*4.5_PR_O*	540.5	9.40	2215.5	856.5	805.6	0.94
RHS_150*100*5_PR_C	541.0	8.35	2358.5	952.6	943.4	0.99
SHS_220*120*6.3_PR_C*	663.0	21.25	4083.0	1604.5	1577.5	0.98
SHS_220*120*6.3_PR_O	662.0	21.35	4108.4	1617.0	1613.7	1.00
SHS_180*6.3_PR_C*	540.0	19.05	4494.0	1756.7	1749.8	1.00

*Buckling occurred on one side due to accidental moment introduction

Because the recorded deformation from the displacement transducers and the strain gauges are different, a correction that combines both sets of measurements was required. Hence, the strain gauges provided the correct Young's modulus slope since they were directly in contact with the column faces while the displacement transducers provided good post-yield information but included the elastic deformation of the end plates leading to an incorrect initial Young's modulus value. A correcting method described by the Centre for Advanced Structural Engineering (Rasmussen & Hancock 1993, Rasmussen 2000) was used (Eqs. 3 and 4). The method consists in a correction factor k that represent the unwanted displacement.

$$k = \frac{L}{2} \left(\frac{1}{E_{LVDT}} + \frac{1}{E_{SG}} \right) \quad (3)$$

$$\delta_c = \delta_{LVDT} - 2kf \quad (4)$$

In Eq. 3, E_{LVDT} represents the initial Young's modulus calculated from the LVDT readings and E_{SG} is the initial Young's modulus calculated from the strain gauges. f represents the applied stress N/A . The corrected end displacement δ_c is then the difference between the LVDT displacements and the set-up displacement. Fig. 5a plots the normalized axial load N/N_{pl} (N_{pl} is the product of the cross-section area A and the tensile coupon yield stress f_y) versus the stubs end

shortening δ before and after correction, and Fig. 5b represents the normalized axial load N / N_{pl} and measured strain $\varepsilon / \varepsilon_y$, ε_y being the strain level at first yield. Local buckling consisted of alternate inward and outward buckles of the stub column constituent plates. Hence, based on the strain gauges location on either the tensile or compressive face of the buckled shape, it can be explained why one of the strain curves reversed direction in Fig. 5a.

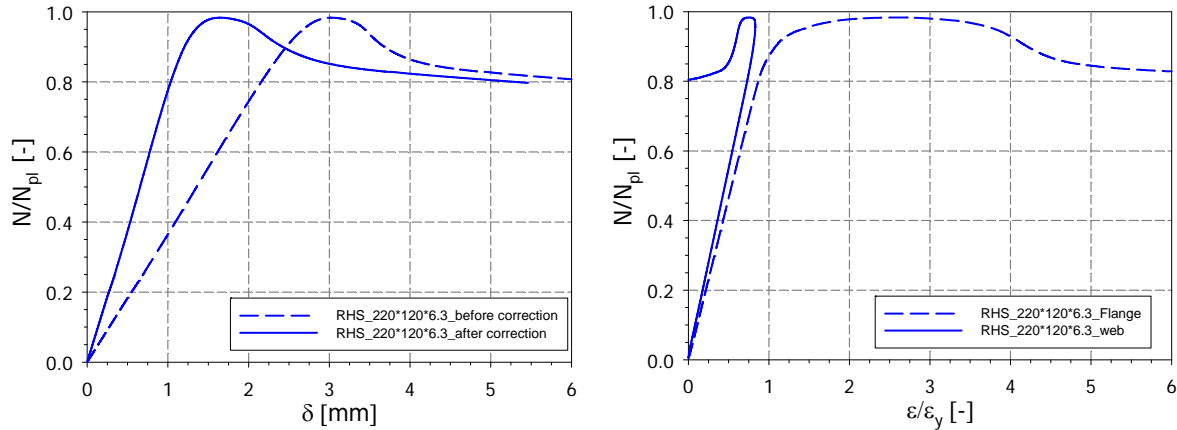


Figure 5: a) Normalized load displacement curve correction – b) Strain gauges measurements

4. 3-point bending tests

Six beams were tested in a typical 3-point bending configuration (Fig. 6). The experimental setup consisted in a simply supported beam on a 30 mm diameter roller. Loading was applied by means of two hydraulic jacks used to generate a concentrated force using two threaded bars connected to a loading beam. Loading was introduced to the specimen with half-round loading point and through a 40 mm thick and 50 mm wide plate to avoid too high levels of stress concentrations.

Various transducers were used to monitor the beam's response:

- load cells were located under each support and under the jacks to record the support reaction and the loading force respectively;
- Inclinometers were fixed at both ends of the beam to measure the beam end rotations;
- Linear variable displacement transducers (LVDTs) were positioned along the beam to record the beam deflection;
- Strain gauges were fixed on the tension flange to measure both its deformation and its curvature.

Loading was applied under displacement control and all readings were taken using an electronic data acquisition system at a 2 Hz pace. Fig. 7 displays the deformed shape of the specimen RHS_150*100*5_SS_3P as an example.

All six beams were tested up to and beyond failure. In most cases, local buckling occurred before beams reached their plastic moment except for the case of the specimen RHS_150*100*8 for which strain hardening was reached and the test had to be aborted before unloading due to high deformations and experimental limitations.

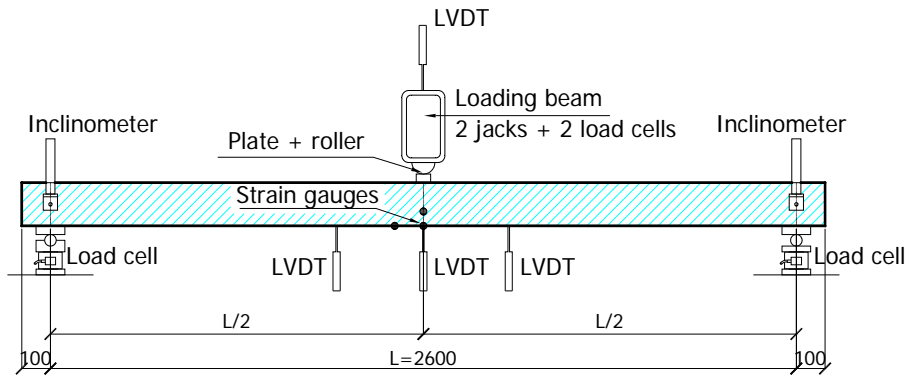


Figure 6: Test setup of the 3-point bending beam (dimensions in *mm*)

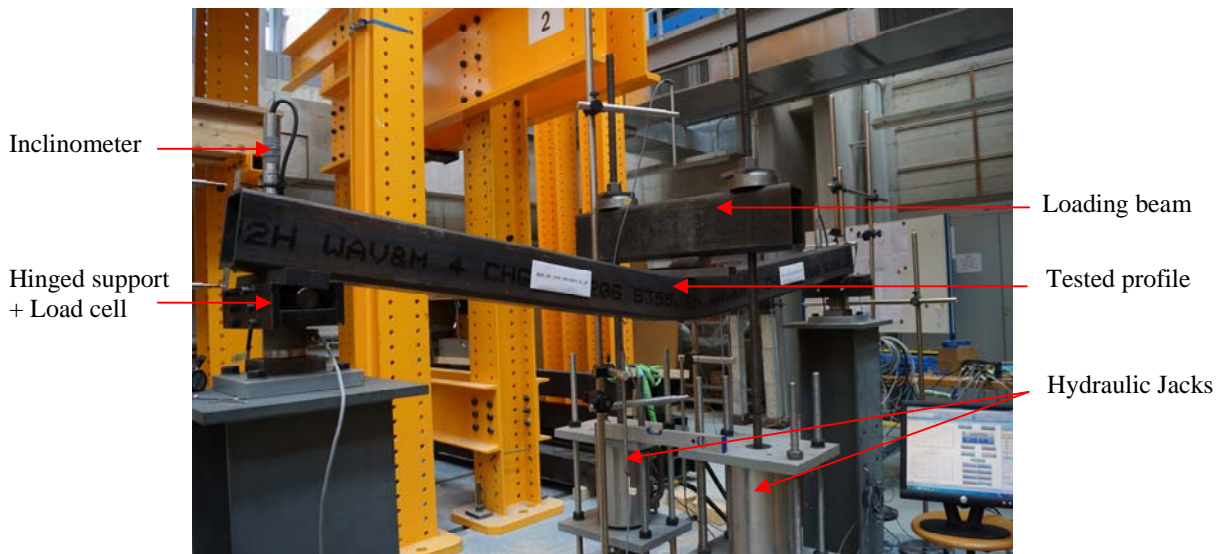


Figure 7: Deformed shape of RHS_150*100*5_SS_3P specimen

The maximum shear rate $V / V_{pl,Rd}$ for the 3-point bending configuration was equal to 32%, so no influence of shear on the obtained result is expected; Fig. 8 shows that the plastic hinge that developed was of limited length due to the moment gradient. Moreover, the onset of local buckling was much localized due to the loading introduction that induced high level of load concentration. Hence, even with the loading applied through a 40 *mm* thick plate, loading was not uniformly distributed on the area of the plate but was applied on the plate extremities in contact with the corners edges. This may explain why beams failed prematurely by reaching 98% of the plastic moment M_{pl} – while being all class 1 in bending – and with an ultimate deflection of 33 *mm*. The RHS_150*100*8_SS_3P – that possess a very stocky section ($\lambda_{rel,p,bending} = 0.2$) – was not influenced by the loading introduction and reached a 139 *mm* deflection at maximum loading.



Figure 8: Onset of local buckling

Fig. 9a presents the moment-rotation curve of three tested beams in which M_{pl} is the plastic moment calculated from measured cross-sections properties, and θ_y is the yield rotation at the beam ends – θ_y is calculated when the middle cross-section first reaches the elastic moment. Fig. 9b represents the total load vs. deflection for these specimens, where P_{pl} is the theoretical plastic collapse load of the system and v is the deflection of the beam at mid-span. According to the plotted curves, it appears clear that all beams failed prior to reaching their plastic capacity, however by a small amount.

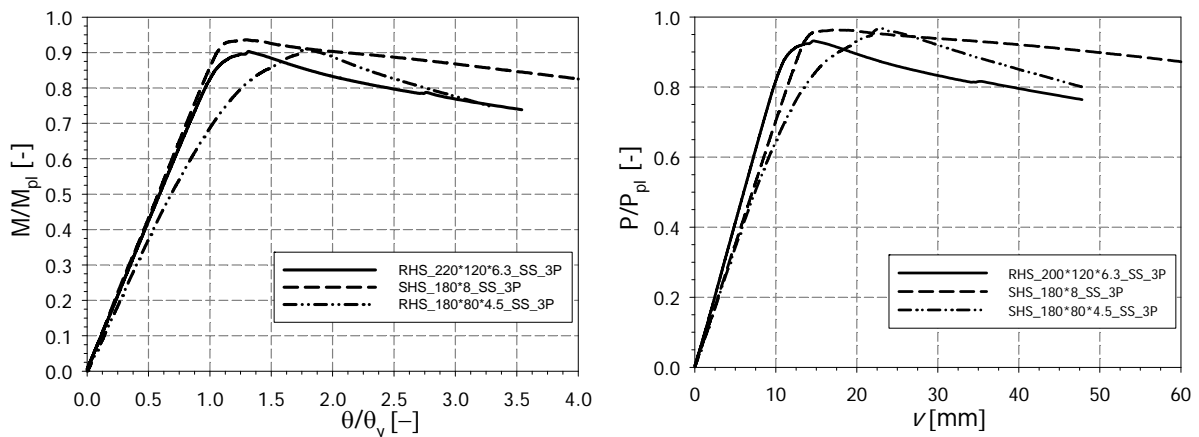


Figure 9: a) Normalized moment-rotation – b) Normalized load-deflection

Table 4 summarizes the non-dimensional ultimate moment M_{ult} / M_{pl} , ultimate load P_{ult} / P_{pl} and their corresponding rotation θ_u and deflection v_u for all tested beams under the 3-point bending configuration.

Table 4: Collapse results for the 3-point bending tests

Test specimen	M_{ult} / M_{pl} (-)	P_{ult} / P_{pl} (-)	θ_u (°)	v_u (mm)
RHS_150*100*8_SS_3P	1.21	1.26	7.27	138.9
RHS_180*80*4.5_SS_3P	0.92	0.97	1.56	22.8
RHS_150*100*5_SS_3P	0.91	0.97	1.95	33.3
RHS_220*120*6.3_SS_3P	0.90	0.93	1.31	14.6
SHS_180*6.3_SS_3P	0.95	0.98	1.35	17.6
SHS_180*8_SS_3P	0.94	0.96	1.30	17.2

5. 4-point bending tests

Six beams were tested under 4-point loading configurations; Fig. 11 shows SHS_180*6_SS_4P specimen at failure. The 4-point bending test setup differs from the 3-point bending arrangement by the insertion of a spreader beam over the tested specimen in order to apply equivalent loads on both loading points located at quarter length of the hinged supports. The low shear ratio V / V_{pl} for the 4-point bending configuration is similar to the 3-point bending one except for the central segment of the specimen which is free from shear forces; shear were not significantly affecting the behavior – no influence of shear on the obtained result was expected, max. shear rate $V / V_{pl,Rd} = 32 \%$. LVDTs and strain gauges have been placed under the loading points and at mid-span to record the beam response accurately as shown in Fig. 10. Load cells were placed under both supports and hydraulic jacks; inclinometers were positioned at the beams' ends.

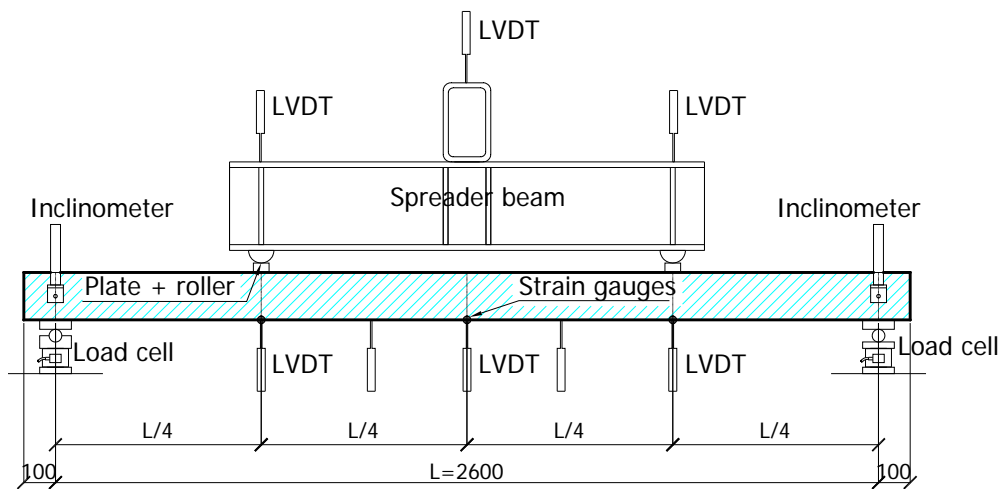


Figure 10: Test setup of the 4-point bending beam

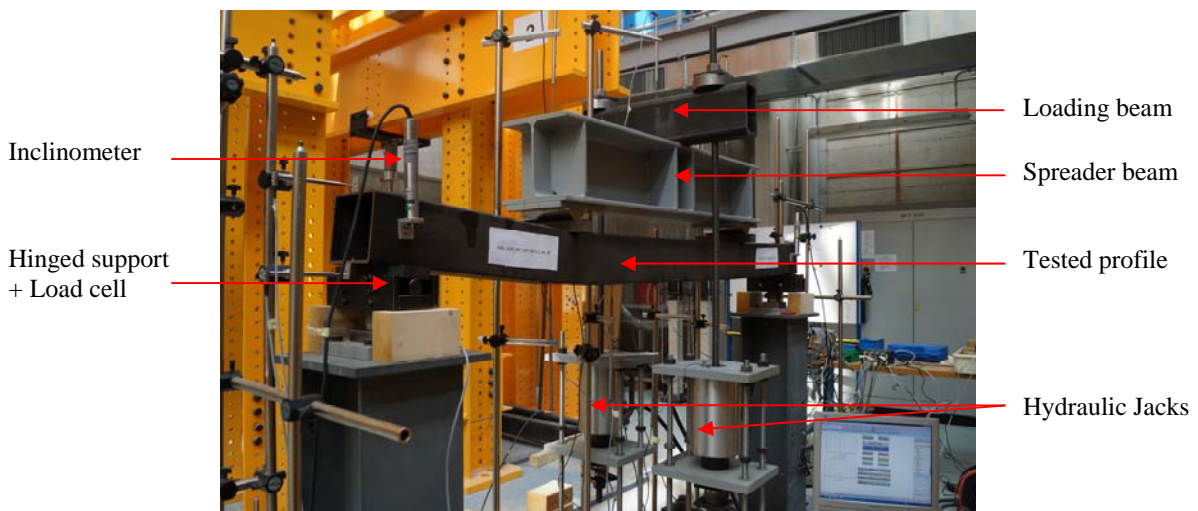


Figure 11: Deformed shape of a 4-point bending beam

During testing, the beams' deflection remained symmetric until the peak loads were reached, i.e. until local buckling failure modes started developing at either the right or left loading point. The failure modes became more pronounced in the post buckling unloading phase leading to an increased unsymmetrical deflection shape as shown in Fig. 13b for RHS_180*80*4.5. The onset of local buckling was localized under the load application (either on the left or right loading point) due to a high level of stress concentration. Fig. 13a shows how the load introduction may have influenced the beam's response, potentially explaining the lower results since local buckling is only pronounced and localized in the vicinity of the 50 mm thick plate.

Fig. 12a represents moment vs. beam end rotations; the divergence between the two curves at the loading points highlights the occurrence of local buckling.

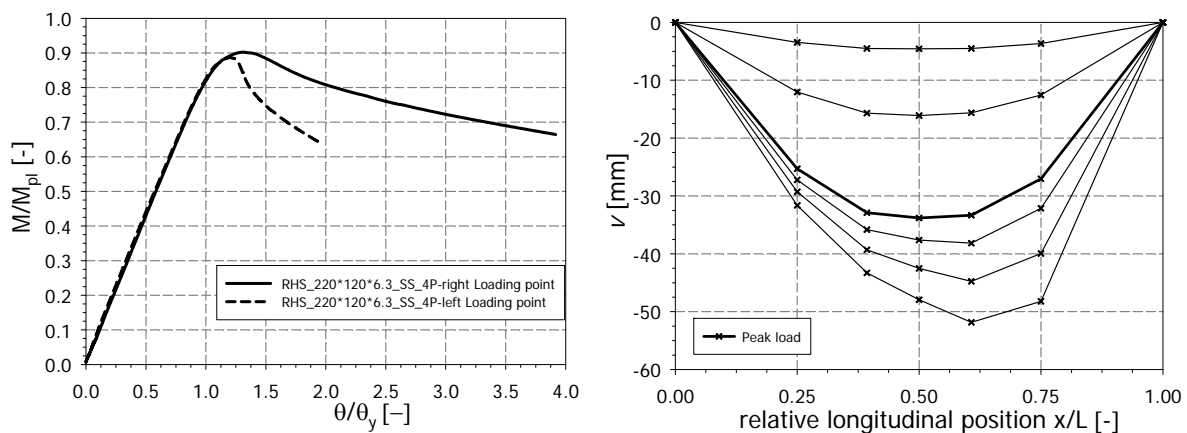


Figure 12: a) Moment-rotation curve of RHS_220*120*6.3 – b) Deflected shape of RHS_180*800*4.5

The ultimate bending moment and the peak load did not fully reach the plastic moment in all tests except for the RHS_150*100*8 specimen who attained strain hardening but where loading was here stopped before reaching the peak load owing to excessive vertical deformations; the beam deflected elastically and without the occurrence of local buckling until reaching a vertical displacement of more than 150 mm (that corresponds to the maximum hydraulic jack capacity) without attaining the system peak load (see Fig. 13b).



Figure 13: a) Onset of local buckling for RHS_180x80x4.5 – b) Deflected shape of RHS_150*100*8

Table 5 summarizes the experimental results for all the tested specimens. Yield rotation θ_y is calculated from the middle segment first reaching the elastic moment, while plastic collapse load P_{pl} is computed for the beam attaining its plastic capacity.

Table 5: ultimate load results for the 4-point bending tests

Test specimen	M_{ult} / M_{pl}	P_{ult} / P_{pl}	θ_u	v_u
	(-)	(-)	(°)	(mm)
RHS_150*100*8_SS_4P*	>1.37	>1.41	>9.09	>149.2
RHS_180*80*4.5_SS_4P	0.93	0.96	1.99	27.0
RHS_150*100*5_SS_4P	0.95	0.99	2.95	47.2
RHS_220*120*6.3_SS_4P	0.90	0.93	1.31	14.0
SHS_180*6.3_SS_4P	0.92	0.95	1.39	16.6
SHS_180*8_SS_4P	0.97	0.91	1.60	20.6

* Specimen didn't reach failure, but test was stopped due to excessive vertical deformations

Both for the 3-point bending and 4-point bending configurations, the theoretical system plastic collapse loads are identical:

$$P_{ult} = \frac{4M_{pl}}{L} \quad (1)$$

The main differences between both configurations are the steepness of the moment gradient and the influence of shear. In the 4-point bending specimens, plastic hinges are theoretically expected to develop somewhere in the middle segment, i.e. between the loading points (constant bending moment). Experimentally, local buckling occurred at the loading points due to a high level of stress concentration and either on the left or right side owing to uneven and askew arrangements. Fig. 14 shows a comparison between the moment rotation curve of the 3-point bending and the 4-point bending configuration for the RHS_220*120*6.3 and the RHS_150*100*5; and Table 6 summarizes all results.

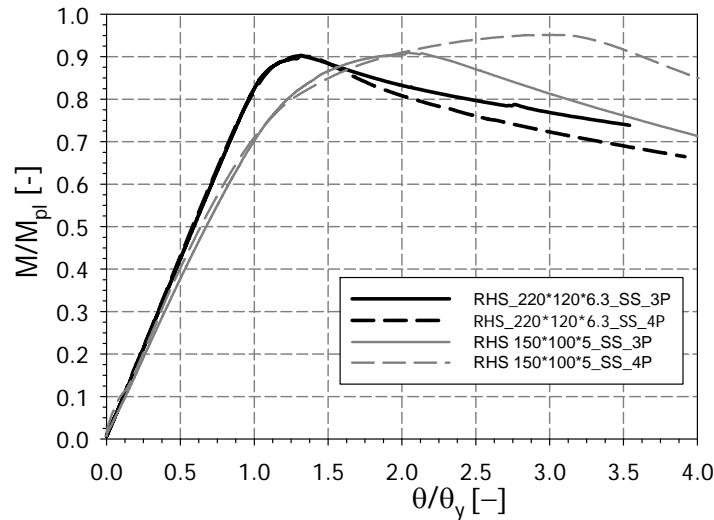


Figure 14: Comparison between 3-point and 4-point configurations of RHS 220*120*6.3 and RHS_150*100*5

Table 6: Comparison of ultimate bending moments between 3-point and 4-point bending configurations

Test specimen	$M_u / M_{pl} (-)$		Difference (%)
	3-point bending	4-point bending	
RHS_150*100*8	1.21	1.37	11.5
RHS_180*80*4.5	0.92	0.93	1.7
RHS_150*100*5	0.91	0.95	4.6
RHS_220*120*6.3	0.90	0.90	-0.1
SHS_180*6.3	0.95	0.92	-3.3
SHS_180*8	0.94	0.97	3.3

6. Propped-cantilever centrally loaded

Five propped-cantilever specimens of 4.8 m span length were tested with the loading being applied at mid-span. Specimens were fixed to a braced support by welding a 30 mm thick plate to the beam's end and then bolting it with 8 10.9 M24 bolts (Fig. 16b). The plate was chosen to be thick enough so as to be considered as perfectly rigid and full penetration welds were realized.

In an attempt to monitor the specimens' strains and curvature at the hinges location without the interference of local buckling on readings, strain gauges were fixed on the tension flange; one was placed on the fixed-end 50 mm away from the plate due to the presence of the weld and another one was placed at mid-span. The inclinometer was attached to the hinged end to measure the beam end rotation and a load cell was placed under the hinged support to measure the support reaction. Loading was introduced in the same way as for the simply supported beams and two load cells were placed under the jacks to record the applied force. LVDTs were placed at mid-span and at quarter span length to measure the beams deflection. The test setup is shown in Fig. 15.

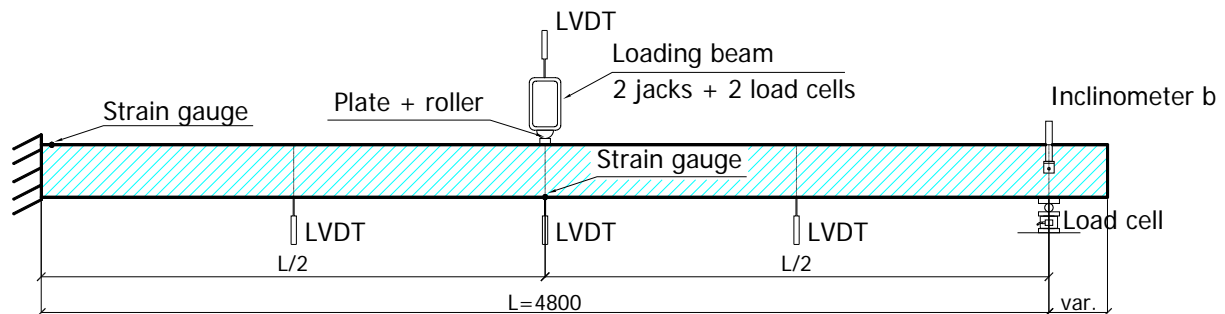


Figure 15: Test setup of the propped cantilever centrally loaded

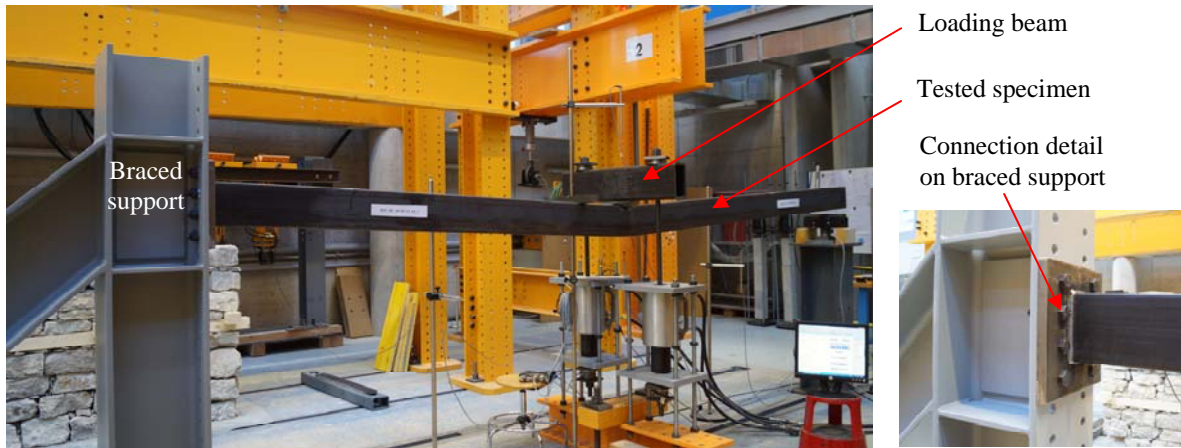


Figure 16: a) Deformed shape of a propped-cantilever centrally loaded – b) Connection detail on braced support

Plastic moment was first reached at the fixed support with the development of a plastic hinge; the bending moment was then redistributed to the middle span until the plastic moment and the peak load were reached. θ_y was calculated when the fixed-end section first reached the elastic moment. The system collapse load was determined in using virtual work principles with the assumption of rigid-perfectly plastic hinges of zero length and an elastic bending moment distribution in between these hinges.

Moment-rotation curves have been plotted using the rotation given by the inclinometer at the hinged end. Results are shown for SHS_180*6.3 in Fig. 17a. As expected, it is shown that, as the test progresses, fixed end moments are higher than at mid-span. System peak load is reached with premature local buckling at mid-span (i.e. before reaching the plastic moment in span). At the fixed end, greater moments were reached due to welding restraints.

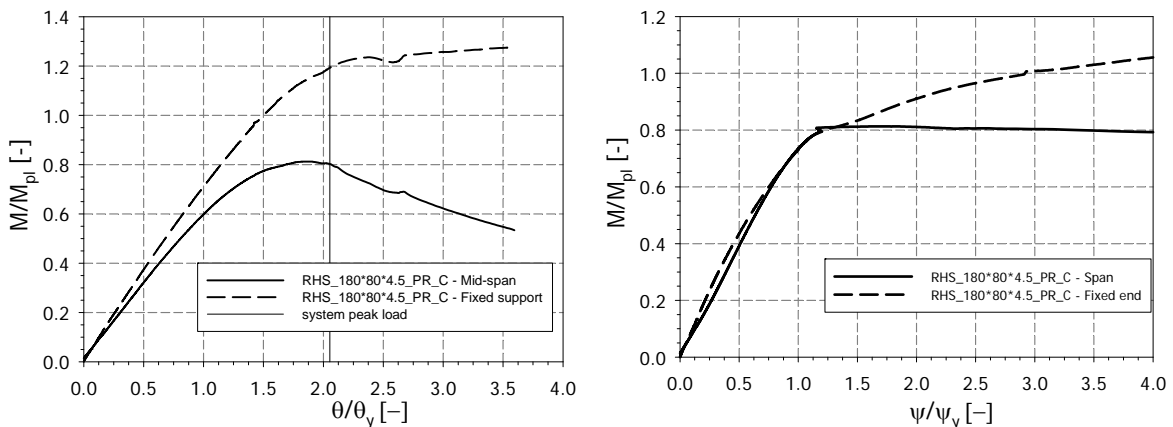


Figure 17: a) Normalized moment - rotation of RHS_180*80*4.5 – b) Moment-curvature of RHS_180*80*4.5_PR_C

Fig. 17b displays the normalized moment-curvature with the yield curvature $\psi_y = M_{el} / EI$ calculated from measured dimensions and material properties. Table 7 summarizes normalized span moments and fixed-end moments along with the system peak load for all the 5 tested specimens.

Table 7: Collapse results for the centrally loaded propped cantilever

Test specimen	$\lambda_{rel, p, bending}$ (-)	$M_{ult/load} / M_{pl}$ (-)	$M_{ult, fixed} / M_{pl}$ (-)	P_{ult} / P_{pl} (-)	θ_u (°)
RHS_180*80*4.5_PR_C	0.34	0.81	1.27	0.95	2.05
RHS_150*100*5_PR_C	0.38	0.96	1.16	1.02	2.99
RHS_220*120*6.3_PR_C	0.35	0.85	1.21	0.88	2.24
SHS_180*6.3_PR_C	0.56	0.87	1.15	0.88	1.34
SHS_180*8_PR_C	0.42	0.87	1.26	0.94	3.16

7. Propped-cantilever off-centrally loaded

Three additional propped-cantilever specimens of 4.8 m span length were tested with loading applied at one third length from the hinged support. This arrangement was performed so that, unlike for the propped-cantilever centrally loaded cases, a plastic hinge would first form in the span and then, due to moment redistribution, failure would occur by the fixed-end reaching the plastic collapse load. Test setup is shown in Figs. 18 and 19. Arrangements for the fixed end, hinged end and loading introduction were performed similarly to the centrally loaded cantilever.

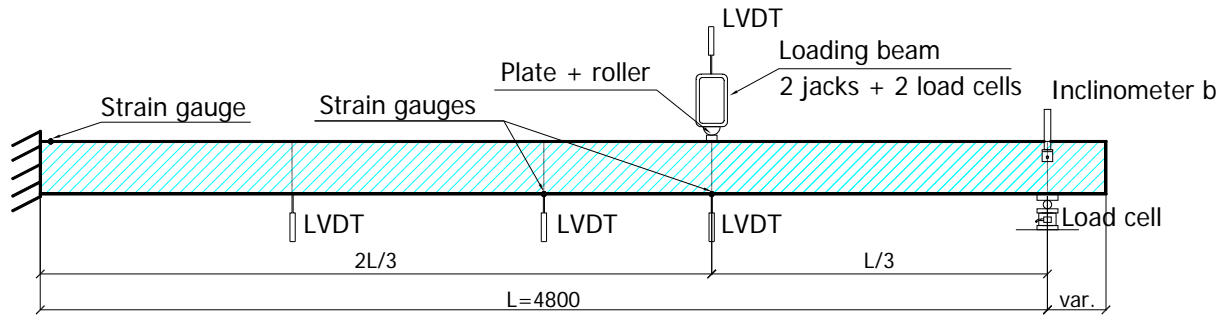


Figure 18: Test setup of the propped cantilever off-centrally loaded



Figure 19: Deflected shape of a propped cantilever off-centrally loaded

As shown in Fig. 20a's moment-rotation plot, span first reached the plastic moment. Failure was then attained in the fixed-end reaching its plastic collapse load. Before the system peak load was reached, span moment was higher than the fixed-end moment after which the span moment decreased and the fixed-end moment increased to reach the plastic moment.

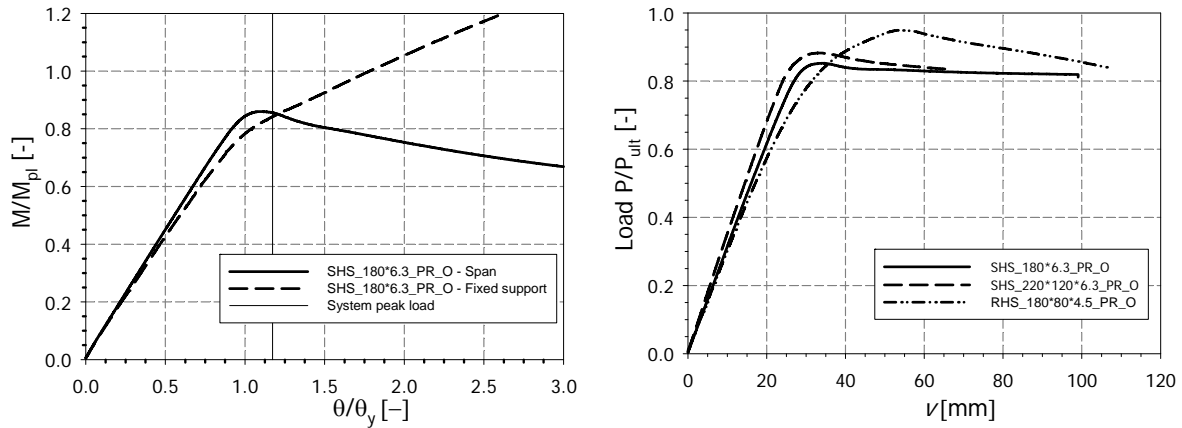


Figure 20: a) Normalized moment-rotation of RHS_180*80*4.5 – b) Normalized total load-span displacement

System peak load occurred at variable vertical displacement levels ranging between 20 mm and 60 mm; load-deflection behaviors of the three propped cantilever off-centrally loaded are plotted in Fig. 20b. The deflection v was measured at the loading point. Table 8 summarizes normalized span moments and fixed-end moments along with the system peak load and corresponding end rotation θ_u for the 3 tested specimens.

Table 8: Collapse results for the off-centrally loaded propped cantilever

Test specimen	$\lambda_{rel, p, bending}$ (-)	$M_{ult, load}/M_{pl}$ (-)	$M_{ult, fixed}/M_{pl}$ (-)	P_{ult}/P_{pl} (-)	θ_u (°)
RHS_180*80*4.5_PR_O	0.34	0.86	1.25	0.85	1.88
RHS_220*120*6.3_PR_O	0.35	0.90	1.03	0.88	1.48
SHS_180*6.3_PR_O	0.56	0.89	1.30	0.95	1.17

8. Conclusions and future steps

Experimental works investigating the available rotation capacity of H.S.S. have been presented. The test program included 4 different configurations, 6 cross-sections dimensions and S355 steel grade profiles from the hot-formed manufacturing process. Tensile tests were performed for all sections. Moreover, seven stub column specimens were tested to measure the level of available ductility of the sections.

The simply-supported test configurations resulted in five out of six sections to experience insufficient plastic rotation capacity, although sections were classified as class 1 (“plastic”) according to Eurocode 3. Moreover, while comparing 4-point and 3-point bending arrangements, uneven experimental setups led to scattered results and no clear tendency could be defined. As for the propped cantilever configurations, the fixed section showed an increase in strength due to welding restraints while the span section did not reach its full plastic moment capacity.

Following the present experimental series, both numerical and analytical investigations will be addressed, with the intention of developing better practical formulations for plastic design. In particular, the development of finite element models and their validation against the test results is currently under way. Then, extensive finite element parametric studies are foreseen, including a wide scope of key parameters such as cross-section shape, steel grade, moment gradient, static system... In fine, revisited ways of defining the possibility to allow for a plastic analysis in practical design shall be made available.

References

- Boeraeve P., Lognard B. (1993). "Elasto-plastic Behaviour of steel Frame works." *Journal of Constructional Steel Research* 27 (1993) 3_21.
- Boissonnade N., Nseir J., Saloumi E. (2013). "The Overall Interaction Concept: an Alternative Approach to the Stability and Resistance of Steel Sections and Members." *Proceedings of the Annual Stability Conference, Structural Stability Research Council*, St. Louis, Missouri, April 16-20.
- Bruneau M., Uang C. & Sabelli R. (2011). "Ductile Design of Steel Structure" - Second edition - Chapter 14.
- Daali M., Korol R. (1995), "Prediction of Local Buckling and Rotation Capacity at Maximum Moment." *Journal of Constructional Steel Research* 32, 1-13.
- CEN (Comité Européen de Normalisation) (2005). "Eurocode 3: Design of Steel Structures, Part 1-1: General rules and rules for buildings (EN 1993-1-1)", Brussels.
- CEN (Comité Européen de Normalisation) (2005). "Eurocode 3: Design of Steel Structures, Part 1-5: Design of plated structures (EN 1993-1-5)", Brussels.
- Gardner L., Saari N., Wang F. (2010). "Comparative experimental study of hot-rolled and cold-formed rectangular hollow sections." *Thin-Walled Structures*, 48:495-507.
- Haaijer G., Thiirliemann B. (1958). "On inelastic buckling in steel." *Journal of Engineering Mechanics Division, Proceedings of ASCE*, 84 (EM2) paper 1581.
- Kato B. (1989), "Rotation Capacity of H-Section Members as Determined by Local Buckling." *Journal of Constructional Steel Research* 13, 95-109.
- Kuhlmann U. (1989), "Definition of Flange Slenderness Limits on the Basis of Rotation Capacity Values." *Journal of Constructional Steel Research* 14, 21-40.
- Liew A. (2014). "Experimental tests on hot-rolled rectangular hollow sections." *Proceedings of the Annual Stability Conference SSRC*.
- Rasmussen K., Hancock (1993). "Design of cold-formed Stainless Steel Tubular Members I columns." *Journal of Structural Engineering, American Society of Civil Engineers*, Vol. 119, pp 2349-2367.
- Rasmussen K. (2000). "Recent Research on Stainless steel Tubular structures." *Journal of Structural Engineering*, Vol. 54, No. 1, pp 75-88.